Annularly Grooved Diaphragm Pressure Sensor With Embedded Silicon Nanowires for Low Pressure Application

Songsong Zhang, Tao Wang, Liang Lou, Wei Mong Tsang, *Member, IEEE,* Renshi Sawada, Dim-Lee Kwong, *Fellow, IEEE*, and Chengkuo Lee, *Member, IEEE*

***Abstract*— We present a nanoelectromechanical system piezoresistive pressure sensor with annular grooves on the circular diaphragm where silicon nanowires (SiNWs) are embedded as sensing elements around the edge. In comparison with our previous flat diaphragm pressure sensor, this new diaphragm structure enhances the device sensitivity by 2.5 times under pressure range of 0–120 mmHg. By leveraging SiNWs as piezoresistors, this improvement is even remarkable in contrast to other recently reported piezoresistive pressure sensing devices. In addition, with the miniaturized sensing diaphragm (radius of 100 μm), the sensor can be potentially used as implantable device for low-pressure sensing applications. [2013-0305]**

***Index Terms*— Piezoresistance, silicon nanowires (SiNWs), pressure sensor, annular groove, low pressure, biomedical.**

I. Introduction

PIEZORESISTIVE effects in silicon & germanium are early reported in 1950s [1]. Unlike the resistance change caused by the volumetric variation in metallic gauges, the large strain induced resistivity change makes silicon as the promising sensing element in mechanical sensor design [2], [3], which can be easily integrated with standard semiconductor processes [4]–[9]. An enormous amount of research efforts on piezoresistive effects has been devoted in both theoretical [10]–[14] and experimental [3], [15]–[18] ways during past decades. As one of the most sophisticated design utilizing the piezoresistive transduction, pressure sensor based on piezoresistive mechanism has been widely adopted in many areas diverse from the automotive industry [19], [20] to the biomedical application [21], [22]. Piezoresistive pressure sensor generally demonstrates a lower non-linearity (NL) than that of the capacitive pressure sensing devices under a small diaphragm deflection range [23]. However, such conclusion does not stand in the case of low pressure sensing. For the conventional flat diaphragm based piezoresistive pressure sensor, when the thinner diaphragm with a large defection is required to sustain the minimum detectable output under a low pressure, the consequent well-known balloon effect will cause a severe degradation in device linearity [24], [25]. In order to solve the problem, a novel boss diaphragm structure, which is configured with a much thicker diaphragm in the center compared to the edge and fabricated based on bulk micromachining, is introduced to concentrate the stress distribution along the beam/rib structure without reducing overall diaphragm thickness and thus remaining a good linearity [25], [26]. Taking the advantage of surface micromachining, Bao *et. al*. proposed a modified boss diaphragm by configuring those rib and groove structures on the front side of sensing diaphragm [27], [28] with an improved process accuracy. Further optimization efforts have been made to improve the boss device pressure sensing performance by optimizing geometry factors, such as dimensions, shapes and the ratio between length and width of such rib and groove structures [23], [29], [30]. Besides, the theoretical study has also been carried out to optimize and predict the device sensitivity and linearity [31]–[33]. Nevertheless the low pressure sensing performance of the boss diaphragm pressure sensor has been reaching its inherent limit with the diaphragm area in the range of mm^2 [23]. A further shrinkage in diaphragm diameter/length will significantly reduce the sensitivity due to a lower resultant resistivity change generated by the deflection induced stress/strain, which is proportional to the square factor of the diaphragm dimension [34]. Hence, other improvement methods have to be developed for a further sensitivity enhancement.

In the past decade, the successful demonstration of implementing nano-scale techniques in both standard CMOS and MEMS technology has been widely reported. Nano-scale materials have been adopted not only for the transistor design [35], [36], but also applied as new sensing element or detection platform [37], [42] for the era of Nano - electromechanical System (NEMS) technology. Among all of promising

Manuscript received September 28, 2013; revised January 22, 2014; accepted March 20, 2014. Date of publication April 11, 2014; date of current version November 25, 2014. This work was supported by the Science and Engineering Research Council (SERC), Agency for Science, Technology, and Research under Grant 1021710159 and Grant 1220103064. Subject Editor A. J. Ricco.

S. Zhang is with the Department of Electrical and Computer Engineering, National University of Singapore, Singapore 117576; and also with the Institute of Microelectronics, Agency for Science, Technology, and Research, Singapore 117685 (e-mail: elezss79@gmail.com).

T. Wang and C. Lee are with the Department of Electrical and Computer Engineering, National University of Singapore, Singapore 117576 (e-mail: elelc@nus.edu.sg).

L. Lou, W. M. Tsang, and D.-L. Kwong are with the Institute of Microelectronics, Agency for Science, Technology, and Research, Singapore 117685 (e-mail: llnusback1023@gmail.com).

R. Sawada is with the Department of Mechanical Engineering, Kyushu University, Fukuoka 819-0395, Japan.

Color versions of one or more of the figures in this paper are available online at http://ieeexplore.ieee.org.

Digital Object Identifier 10.1109/JMEMS.2014.2313635

nano-scale sensing elements, both fundamental property and fabrication technology of silicon nanowires (SiNWs) have been well studied over the last decade [43]–[50]. Tremendous experimental efforts have also been carried out for optimizing the performance of nanowires as a piezoresistive sensing element [51], [52]. With the proven stability [53], [54] and excellent piezoresistive sensing performance reported [55], [56], single crystal SiNWs have been successfully implemented into NEMS sensors for various applications (e.g. tactile sensor, mechanical switch and etc.) and resulted in remarkable outcomes [57]–[59].

In this paper, by leveraging the higher concentrated stress profile contributed by annular groove structures on a thin diaphragm (0.5 μm thick in hinge region and 3 μm thick in the rest of the diaphragm area), we successfully demonstrate a new annularly grooved diaphragm pressure sensor using embedded SiNWs as piezoresistors for the low pressure application. The reported proof-of-concept NEMS pressure sensor with miniaturized sensing area, which suits the demands of minimum invasive implantation, can be potentially used for bio-medical applications under a low pressure range.

II. Design Consideration

As aforementioned in the introduction, it is difficult to obtain a good low pressure sensing characteristics by simply reducing the diaphragm thickness of the conventional flat diaphragm structure. A balance between excellent sensing resolution and optimum linearity is always the key concern. Thus, the previously reported flat pressure sensor [60] has to be redesigned for the purpose of low pressure detection. Rather than complicated diaphragm structures as reported [23], [27], [29], [33], only the simple structure with annular grooves and ribs around the diaphragm edge is chosen to simplify the fabrication process as well as to prove the concept. The device drawing of our annularly grooved diaphragm pressure sensor is shown in Fig. 1(a) with the detailed groove geometry and diaphragm cross section provided in inset I & II (In Inset II, the top passivation layer (Si_3N_4) has been turned into transparent for a clearer view). According to the previous study reported by Yasukawa *et. al*. [61], the induced surface strain of the both circular boss diaphragm (structure – B) and circular boss diaphragm with rib (structure – B&R) can be expressed as following:

$$\varepsilon_{\text{total}} = \frac{3h_r\xi}{w_g}\omega + \frac{\pi^2}{16(1+\beta)w_g^2}\omega^2 \tag{1}$$

$$\& \ \beta = \frac{h_r w_r E_r + h(\pi a E_d - w_r E_r)}{\pi a w_g k_s} \tag{2}$$

Where ε_{total} is the total induced surface strain. h_r and h are the thickness of the rib/center boss and hinge region, which is the remaining diaphragm portion below groove structures and connected to the device substrate. ω is the diaphragm deflection, w_g is the width of the groove, w_r is the width of rib, and ξ is the nondimensional coordinate of the gauge position (varies from 1 to -1). β is defined in (2), a is the radius of the diaphragm, E_d and E_r are the equivalent Young's modulus of the diaphragm and rib respectively. k_s is the support stiffness.

In their study, the total induced strain can be treated as the combination of rib/beam bending strain (the 1st portion of the equation (1)) plus the diaphragm deforming strain (the 2nd portion of equation (1)). When only structure – B is applied, the equation can be simplified by equal h_R to h. Therefore, for structure – B&R, the sensitivity can be further improved by reducing the thickness at the hinge region. In another word, the thickness at the boss region is virtually increased. In order to validate the assumption of a boss structure, the thickness of the center boss region should be at least 6 times of the thickness of the hinge (the remaining thickness at groove region). Additionally, one of initial conditions for the equation of boss structure assumes a negligible bending moment at the center boss region under a given applied pressure. Thus, the mechanical stiffness at the center boss has to be the much higher than that of the hinge region. Such stiffness can be characterized by flexural rigidity as expressed in equation (3).

$$D = \frac{Eh^3}{12(1-\nu^2)} \tag{3}$$

Where E is the equivalent Young's modulus of the structure and h is the structure thickness and ν is the Poisson's ratio. With a fixed equivalent Young's modulus, the stiffness is highly dependent on the diaphragm thickness. Therefore, the thickness is usually above 10 μm for a good linearity according to the literature [62], especially for those with the center boss structure [23]. In our case, however, the initial diaphragm does not perfectly match the boss configuration (the ratio of the thickness between center and hinge area is only 5.5) and the center thickness may be too thin ($\sim$3 μm as indicated in Fig. 1 Inset II) to be considered as a rigid structure for minimizing center deflections. Nevertheless, the analysis of equation (1) does provide the design guideline for the reconfiguration of original diaphragm structure and to demonstrate the concept of the sensing capability for the SiNWs based NEMS device under a low pressure. The location of piezoresistors (SiNWs in our case) is usually placed along beam/rib region and buried away from the neutral axis. In our design, SiNWs are laid on the BOX layer (buried thermal oxide) and close to bottom surface as shown in Fig. 1, Inset II. In addition, the thickness of rib should be the same as that of the center diaphragm. As indicated in the equation (3), hence, a smaller deflection will be observed at rib region compared to the deflection at hinge region and a resultant lower non-linearity will be accomplished [27].

Besides the sensitivity and linearity improvement for structure – B&R, another advantage of such structure is to minimize the fabrication variation due to the front to back side misalignment. As a result of the front side fabrication, the groove can be patterned with a relatively higher accuracy compared with the result based on backside alignments. Moreover, the well aligned groove re-defines the original stress distribution profile confined by the edge of the conventional flat diaphragm structure, which is released by the back side process. Such stress re-distribution is realized by concentrating the stress along the rib region [29]. Consequently, less performance variations among each individual die is ensured during the final device characterization. The detailed experimental result

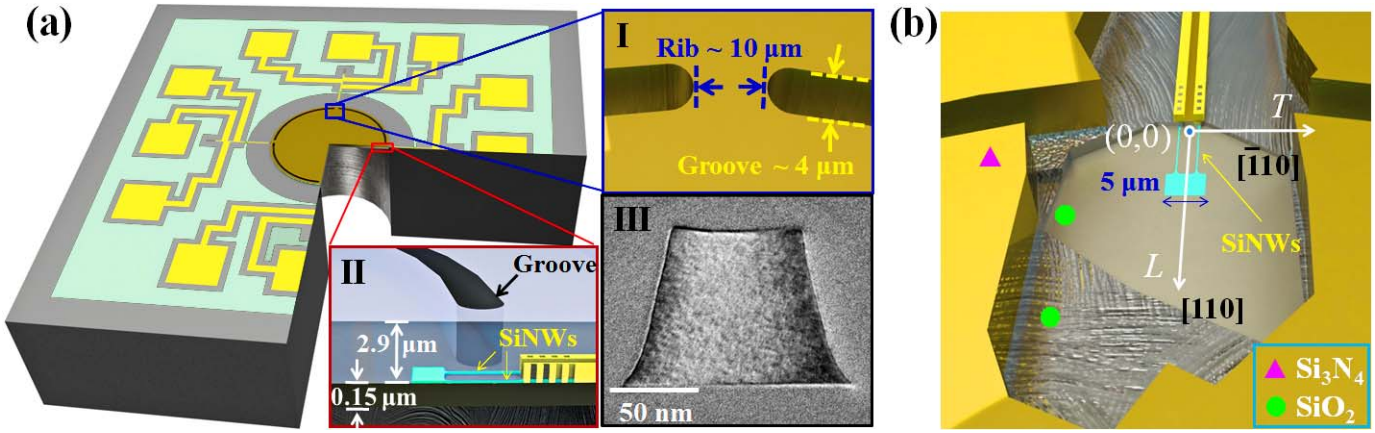

Fig. 1. (a) The schematic of SiNWs embedded pressure with groove and rib structures on the circular sensing diaphragm (released from the back side); (b) The spot view in the location of SiNWs after etching back top passivation layers (2.5 μm Si_3N_4 and 0.4 μm SiO_2). SiNWs are patterned along [110] direction as indicated by white arrow. Inset I: the close-up view of the micro-groove; Inset II: the cross-section view of the multilayer diaphragm. Inset III: a TEM image for the cross-section of the nanowire.

for minimizing the device variation will be elucidated in section IV. Additionally, to achieve a better sensitivity and optimum non-linearity, both groove and rib width should be kept as narrow as possible [27], [29]. However, the practical consideration limits the minimization of both groove and rib width in our case. As shown in Fig. 1(b), the width of the paddle connecting two nanowires is around 5 μm. To tolerance alignment errors and etching processes, the width of rib and groove are set to be 10 μm and 4 μm respectively (Shown in Fig. 1 Inset I).

Apart from diaphragm geometry parameters, the nanowire itself also needs to be optimized for better sensing performances. The p-type impurity concentration is firstly designed within the range of 1 to 3 $\times$ 10^{18} cm^{-3}. This is to make sure the optimization of piezoresistive effects, which have to be balanced between a reasonably large piezoresistive coefficient (lower the impurity higher the value) and a relatively acceptable temperature dependency of the piezoresistor (higher the impurity less the temperature induced variation) [12], [16], [18]. It has also been reported that the non-linearity component of piezoresistance is also related to the impurity concentration [25], [31] due to the non-proportional relationship between the splitting of valence band states caused by the energy band shift between heavy and light hole [63]. Details on temperature effects will be discussed in the following chapter. In addition, the cross-section geometry is another important factor to maximize the piezoresistance effect of SiNWs [56]. The ideal cross section view of SiNWs should be a square shape such that the plasma induced damage to the nanowire sidewall can be minimized. However, due to the imperfection of photolithography process, the practical shape of the cross section is always trapezoidal (as shown in Fig. 1 Inset III). Furthermore, the resistance change due to the longitudinal [defined by L in Fig. 1 (b)] stress component should be maximized and the resistance change caused by transverse [defined by T in Fig. 1 (b)] stress component has to be kept as minimum for a better overall performance under a given applied normal pressure. The expression of total resistance changes is shown as below:

$$\frac{\Delta R}{R} = \pi_L \sigma_L + \pi_T \sigma_T \tag{4}$$

Where π_L and π_T are the piezoresistance coefficients along longitudinal and transverse direction, respectively, which for silicon in this orientation have opposite polarities. σ_L and σ_T are the stress components along each direction. As explored by T. Toriyama *et. al.* [56], the longitudinal piezoresistance effect can be enhanced by reducing the cross section area of the silicon nanowire. On the other hand, the effect of transverse piezoresistance can be minimized by proper design of the aspect ratio, which is defined as the nanowire thickness divided by its mean width. With the aspect ratio close to 1 (thickness $\approx$ width), the stress transmission ratio $= (\sigma_T/\sigma)$ along the transverse direction can ideally approximate to 1, therefore, maximizing the transformation of stress component in the longitudinal direction. Here, σ is the normal stress applied to the substrate. Meanwhile, the change of aspect ratio does not affect the stress component along the longitudinal direction. The detailed process for the optimization of the SiNWs cross section geometry will be described in the next chapter.

III. Device Fabrication

As shown in Fig. 2(a), the device fabrication starts on (100) plane single crystal SOI wafer with the device layer of 117 nm and BOX layer (buried thermal oxide) of 145 nm. The global implantation with a boron dosage of 1 $\times$ 10^{14} ion/cm^2 is conducted followed by a 30 seconds rapid thermal annealing (RTA) process at 1050 °C for dopant activation. The resultant final impurity concentration of SiNWs is around 3.5 $\times$ 10^{18} cm^{-3} [64]. The focus exposure matrix process is carried out on test wafers to optimize the exposure recipe prior to the photolithography process. The first photolithography is then performed using the stepper mask (feature projection) based on the result from the focus exposure matrix with the critical dimension ~150 nm after developments. The photoresist is then trimmed for 60 seconds by plasma-induced feeding gas

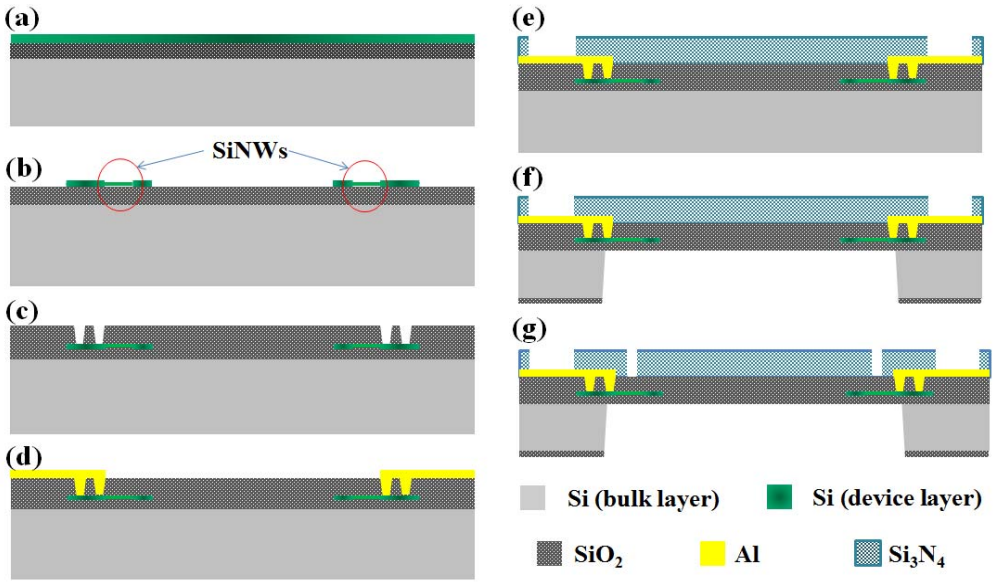

Fig. 2. Device process flows of SiNWs embedded pressure sensor with grooves on the front diaphragm. (a) the starting (100) plane SOI wafer; (b) the formation of SiNWs along ⟨110⟩ direction; (c)-(d) Deposition of 1st passivation layer (400 nm PECVD SiO_2) and metallization; (e) Deposition of 2nd passivation layer (2.5 μm PECVD Si_3N_4) and bond pad opening; (f) backside DRIE for the diaphragm release; (g) the pattern of grooves by etching away Si_3N_4 on the front side diaphragm.

($He/O_2 + N_2$) and result in the minimum feature size of 110 nm in final. The plasma etching is processed to form the SiNWs along <110> direction as shown in Fig. 2(b). This orientation of SiNWs is chosen to maximize the piezoresistive effect of p-type SiNWs on (100) plane [65]. With further thermal dry oxidation at 875 °C for 2 hours, SiNWs with an average cross section of 90 nm × 90 nm (resultant aspect ratio ≈ 1 as shown in inset III of Fig. 1) and various lengths (1 μm, 2 μm, 5 μm and 10 μm) are fabricated. The 2nd implantation with a boron dosage of 1×10^{15} ion/cm^2 is conducted at only the contact and paddle region. After deposition of 1st passivation layer (400 nm of SiO_2), via is drilled through top SiO_2 layer to the bottom highly doped silicon layer [Fig. 2(c)]. A 750 nm Al plus another 25 nm TaN layer (serving as adhesion layer between Si and Al) are sputtered and patterned to form the electrical connection [Fig. 2(d)]. Sequentially, A 2.5 μm thick low stress (~84 MPa) Si_3N_4 is then coated by using plasma-enhanced chemical vapor deposition (PECVD) to compensate the residual stress from beneath oxide layers. As a result, the flat diaphragm with initial deflection less than 100 nm is targeted [60]. After bond pad opening shown in Fig. 2(e), the front side sensing diaphragm is successfully defined through the back-side deep reactive-ion etch (DRIE) with the BOX layer (buried thermal oxide) as an etching stopper shown in Fig. 2(f). However, due to the non-uniformity of inductively coupled plasma etching, the deviation of final released diaphragm is as large as 12 % [as shown in Fig. 7(a)] from the target diaphragm (diameter of 200 μm), especially at the center and edge ring shaped area around the 8-inch wafer. Finally the front side annular groove is defined with a contact glass mask and patterned through the etching process on the 2.5 μm Si_3N_4 cladding layer in an annular region along the diaphragm edge. The beneath SiO_2 layer (~500 nm thick) is used as the etching stopper [Fig. 2(g)].

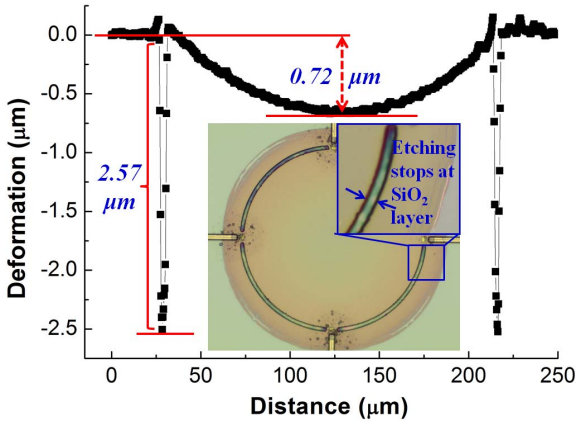

Fig. 3. The plot for the initial deflection of the annularly grooved diaphragm. The diaphragm deforms downward and forms a concave shape. Inset shows the optical image of the pressure diaphragm and a zoom-in view of the groove.

IV. Experiment Result and Discussion

A. Sensitivity and Linearity

The optical image of the release diaphragm with groove and rib structures is given in the inset of Fig. 3. The zoom-in image on the groove region indicates a successful etching stop on beneath SiO_2 layers and this is further verified by capturing the diaphragm topography using white light interferometer (WYKO NT3300). With the depth of groove about 2.57 μm, the over etch of SiO_2 layer (~70 nm) is about 12% of the total thickness of SiO_2 layers (400 nm PECVD SiO_2 layer plus 145 nm thermal SiO_2 layer). However, it is also plotted as the trade-off of a significantly reduction in the hinge region (thus the reduction of the flexural rigidity), the initial diaphragm deflection of 0.72 μm is found and it is about a quarter of the total diaphragm thickness (~3 μm). To further understand the initial diaphragm deflection, the simulation on

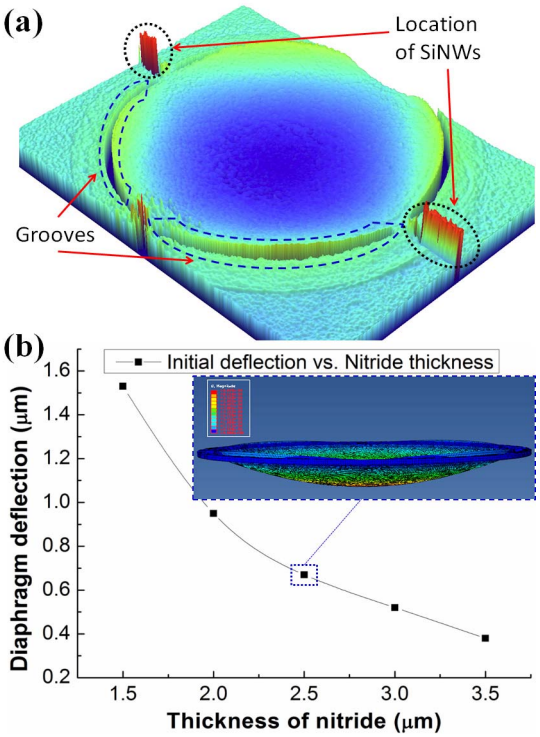

Fig. 4. (a) The surface profile captured by Wyko white light system and (b) the simulated relationship between the nitride layer thickness and the initial diaphragm deflection. The inset shows the simulated diaphragm shape (concave) when a 2.5 μm thick nitride is used as the cladding layer.

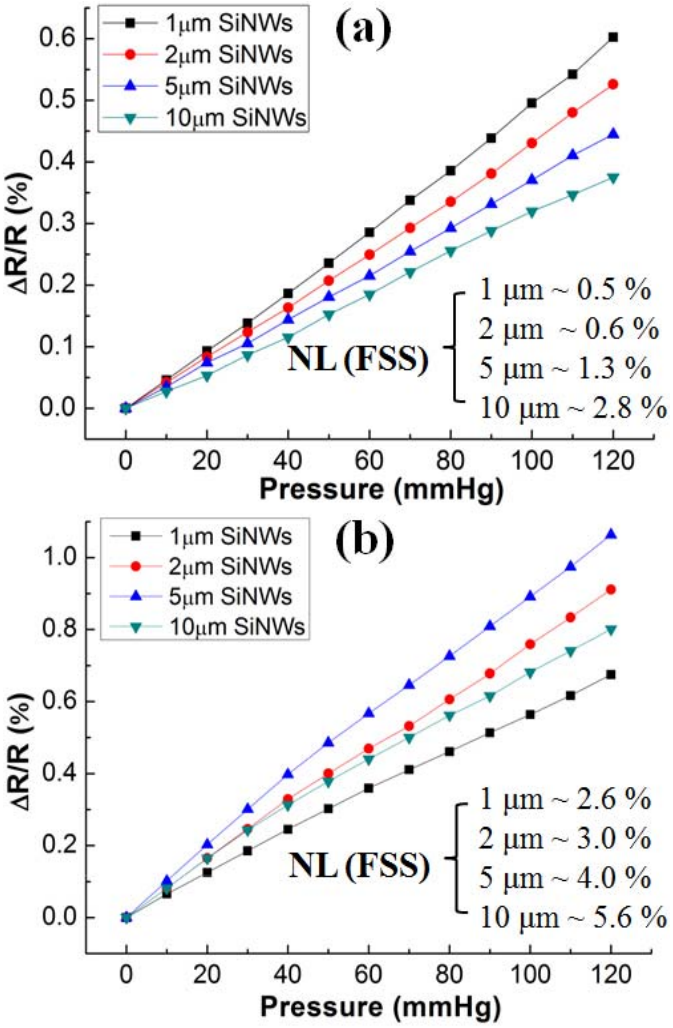

Fig. 5. Plots of the percentage changes of resistance ($\Delta R/R$ *(%)*) with respect to pressure changes for (a) the conventional flat diaphragm SiNWs pressure sensor and (b) the annularly grooved diaphragm SiNWs pressure sensor. The calculated nonlinearity for pressure sensors with different lengths of SiNWs (1 μm, 2 μm, 5 μm and 10 μm) is given in insets.

the effect of residual stresses contributed by the multi-layered diaphragm (named in the sequence from bottom to top: buried thermal oxide layer, PECVD oxide layer and PECVD low stress nitride layer) is conducted. The simulation is conducted by using Abaqus 6.10 and all parameters used in simulation are listed in Table I. The result of diaphragm deflections with respect to different thicknesses of nitride layer is plotted in Fig. 4(b) and it reveals the inverse proportionality between the diaphragm deflection and the cladding nitride layer thickness. In addition, both the simulation result [inset of Fig. 4(b)] and the measurement data [Fig. 4(a)] indicate a concave shape diaphragm. The value of the simulated deflection (~0.67 μm) is very close to the experimental data (~0.72 μm) captured by Wyko white light system. As a rule of thumb, a deflection less than 10 % of the total diaphragm thickness will introduce a mechanical non-linearity of 0.2 % and a deflection less than 30 % of the total thickness will cause a non-linearity component as large as 2 %. For a deflection large than 30% of the diaphragm thickness, this assumption of the small deflection principle is no longer valid [66].

To verify the performance difference of the SiNWs based pressure sensor with the new annularly grooved diaphragm in contrast to the previously reported flat diaphragm counterpart, the percentage of resistance changes over the initial resistance (when no pressure is applied) are measured in the form of $\Delta R/R$ *(%)* by varying pressure changes on X-axis. The testing is firstly conducted under room temperature (25 °C) with supply voltage of 0.5 V. The resistance change is measured by the semiconductor characterization system (Keithley 4200-SCS) with the compressed air source applied by the pressure regulator (ALICAT PCD Series) from the backside of the device (please refer to [60] for more detailed testing setups). As a result, piezoresistors will experience a uniform tensile stress. Fig. 5(a) illustrates the resistance change of the traditional flat diaphragm pressure sensor, the maximum average percentage change (~0.6 %)

TABLE I
MATERIAL PROPERTIES APPLIED IN THE FINITE ELEMENT METHOD (FEM)

Material	Young's modulus	Poisson's ratio	Residual stress (MPa)	Density (g/cm^3)
Si_3N_4	170 GPa	0.27	85 (tensile)	3.44
SiO_2	60 GPa	0.20	-250 (compressive)	2.65

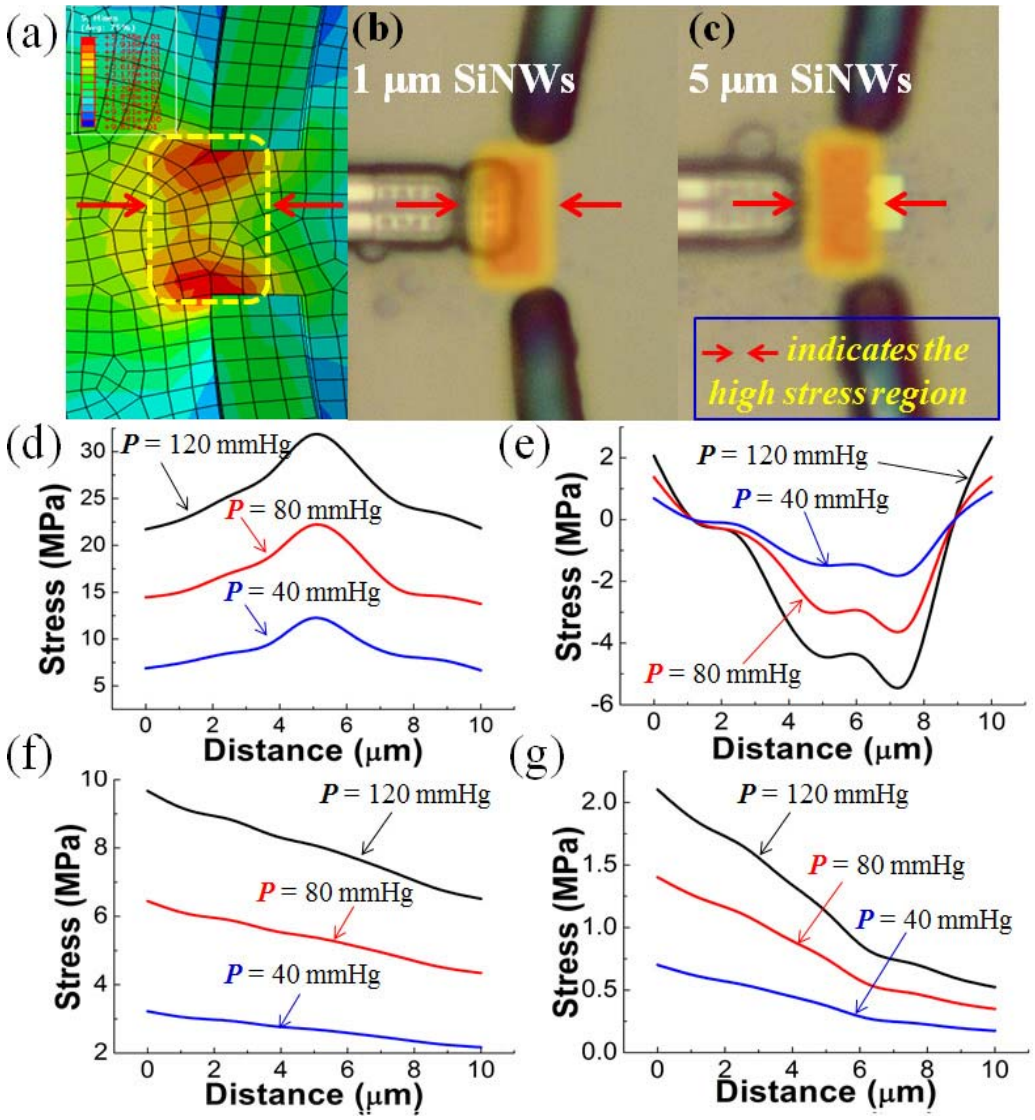

Fig. 6. (a) Illustration of high stress region captured from FEM, (b) - (c) zoom-in optical images of rib region for 1 and 5 μm SiNWs designs respectively. Simulation results of (d) - (e) extracted stress distributions for both longitudinal and transverse stress component along L-direction of the grooved diaphragm pressure sensor, (f) – (g) extracted stress distributions for both longitudinal and transverse stress component along L-direction of the conventional flat diaphragm pressure sensor.

occurs for the 1 μm SiNWs embedded pressure sensor among other designs with longer length of embedded SiNWs. The reasonable explanation has been addressed based on changes of stress distribution profiles along the radial direction of the diaphragm [60]. When SiNWs are located away from the diaphragm edge, the average longitudinal stress experienced along the nanowires gradually decays as the stress distribution profile shown in Fig. 6(f). In the case of the grooved diaphragm pressure sensor, the maximum average percentage change of 1.07 % for 5 μm SiNWs pressure sensor is observed [Fig. 5(b)]. In contrast to the 5 μm SiNWs embedded flat diaphragm pressure sensor, the improvement of percentage changes is about 2.5 times and this change is in a good agreement with the finding of the increment of the average stress distribution along longitudinal direction from the simulation.

The non-linearity (NL) for both the flat diaphragm and the grooved diaphragm pressure sensor with different lengths of SiNWs over full-scale span (FSS) are also calculated based on equation (5) [63] and provided in insets.

$$NL = \frac{R(\mathrm{T}) - \{[R(\mathrm{T}_m) - R(0)](\mathrm{T}/\mathrm{T}_m) + R(0)\}}{R(\mathrm{T}_m) - R(0)} \quad (5)$$

Where, $R(0)$ & $R(\mathrm{T})$ are output resistance values at the initial condition (pressure = 0) and a given pressure status (pressure = T), respectively. The pressure varies from 0 to T_m (maximum pressure applied). As predicted from the initial deflection profile plotted in Fig. 3, a larger non-linearity is introduced after reconfigurations of the original flat diaphragm structure. Beside an extra increment of non-linearity, an obvious sensitivity shift from the previously reported flat diaphragm with 1 μm SiNWs to the currently reported grooved diaphragm with 5 μm SiNWs is observed. To understand this shift, the FEM is conducted and zoom-in views of the

beam/rib structure are also provided in Fig. 6(b) and (c) with a reference image showing the high stress distribution region from FEM [Fig. 6(a)]. As depicted in Fig. 6(a), the highest stress region is located slightly behind (around 2 μm behind) where groove structures are fabricated along the rib. The location of 1 μm SiNWs [shown in Fig. 6(b)] is out of the high stress region, whereas, 75∼80% portion of 5 μm nanowire [shown in Fig. 6(c)] is completely merged within such high stress region. The detailed stress distribution profiles along the rib [*L*-direction defined in Fig. 1(b)] under three different external pressures are plotted in Fig. 6(d). The point (*0, 0*) [indicated in Fig. 1(b)] is defined as the origin for the *X-axis* (distance). With the same explanation, the average stress distributed along 2 μm SiNWs is higher than that of 1 μm SiNWs design but lower than the average stress of 5 μm SiNWs design. For the 10 μm SiNWs, however, it is too long to be entirely confined within the high stress region, thus, experiencing a lower average stress. In addition, the transverse stress distribution profile with the same origin, span and direction are plotted in Fig. 6(e) as well. Unlike the linearly decayed stress distribution from edge (tensile stress) to the center (compressive stress) in the case of flat diaphragm pressure sensor [indicated in Fig. 6(g)], it is worth noting that the stress distribution profile is no longer linear after fabrication with grooves. The stress profile ramps from the small tensile down to relatively larger compressive region and reaches its maximum (compressive) at distance about 7 μm away from the origin. It then ramps up again to tensile stress region. Although this stress change does not dominate the difference in the final resistance value, it theoretically reduces the average transverse resistance changes by approximate 10%, if the same length (7 μm) of the nanowires is allocated within exact the compressive stress region. Hence it leads to improvement of the total resistance change as defined in equation (4). However, the larger transverse stress will also cause an increased non-linearity component regardless of the stress polarity (both compressive and tensile) [63], therefore, such compressive stress profile may also provide a negative contribution to the device linearity. To further understand the non-linearity component, a more closed-from expression of non-linearity between an applied pressure and the final resistance change of a given piezoresistor can be described as the following [61]:

$$NL_{p-R} = NL_{\varepsilon-R} + NL_{\omega-\varepsilon} + NL_{p-\omega} \tag{6}$$

Where NL_{p-R} is the total non-linearity component between applied pressure and final resistance changes; $NL_{p\text{-}R}$ is non-linearity component introduced between strain/stress and resistance changes; $NL_{\omega\text{-}\varepsilon}$ is non-linearity component introduced between deflection and strain changes; $NL_{p\text{-}\omega}$ is non-linearity component introduced between applied pressure and mechanical deflection changes. We have examined non-linearity components contributed by both $NL_{p\text{-}\omega}$ (∼2 % due to the initial diaphragm deflection) and $NL_{\varepsilon\text{-}R}$. The $NL_{\omega\text{-}\varepsilon}$ is usually small and can be removed by an external circuit. For instance, by applying the Wheatstone bridge structure, $NL_{\omega\text{-}\varepsilon}$ can be further minimized [61].

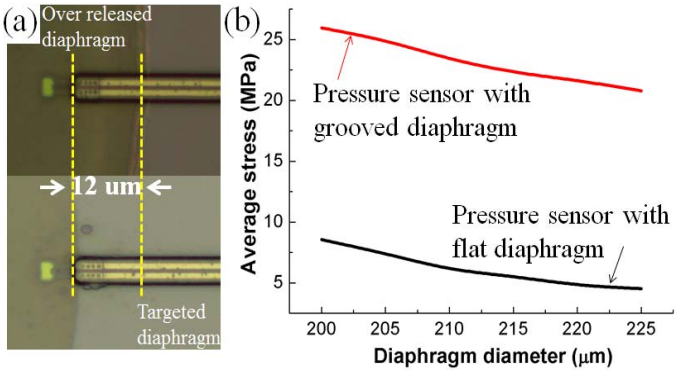

Fig. 7. (a) Optical images of over-release diaphragm (top) and targeted diaphragm (bottom) with embedded 5 μm SiNWs, (b) Simulation results of extracted average stress along 5 μm SiNWs for both grooved and flat diaphragm pressure sensor with respect to the diaphragm diameter variation.

B. Improvement on Process Variations

Another aforementioned advantage of the groove structure is the reconfiguration of the stress distribution. As illustrated in Fig. 7(a), the backside release process has introduced large fabrication variations and the over-release of the diaphragm can be up to 12% of the targeted dimension (diameter of 200 μm). As a consequence, the performance of the released device varies significantly from die to die. The average stress distributed along 5 μm SiNWs with respect to the diaphragm size variation for both the flat and the grooved diaphragm pressure sensor is extracted by using FEM [plotted in Fig. 7(b)]. For a flat diaphragm structure, the amount of average stress drops more than 45 % by varying the diaphragm diameter from 200 μm up to 225 μm. In case of the grooved diaphragm, such diameter variation affects the average stress change up to only 18 %. The FEM is conducted based on a linear perturbation model. For further verification, the experiment is conducted on different pressure sensor samples (n = 10) with various diaphragm diameters. Output resistance variations for 5 μm SiNWs embedded in both flat and groove diaphragm pressure sensor are shown in Fig. 8. The blue curve with error bars reflects results for the flat diaphragm pressure sensor (referring to bottom *X* and left *Y*-axis) with the deviation of resistance changes up to 33% of its mean value at pressure of 120 mmHg. On the other hand, as plotted in red curve with error bars (referring to top *X* and right *Y*-axis), the variation of diaphragm size only introduces 14 % of performance differences to the annularly grooved pressure sensor within the same pressure range. The obvious improvement of the device sensing performance over process variations is hereby reported and it is contributed by the groove structure, which forces the stress distribution along the rib.

Here, the reported device is just the proof-of-concept for the sensing capability of SiNWs embedded sensor under a low pressure and the design has not been completely optimized yet. Further sensitivity improvement can be realized by changing circular diaphragm to a square shape. This change may lead to the sensitivity improvement up to 60% base on flat plate design theory [66]. Additionally, the optimum location of SiNWs with respect to the annular groove has not been determined.

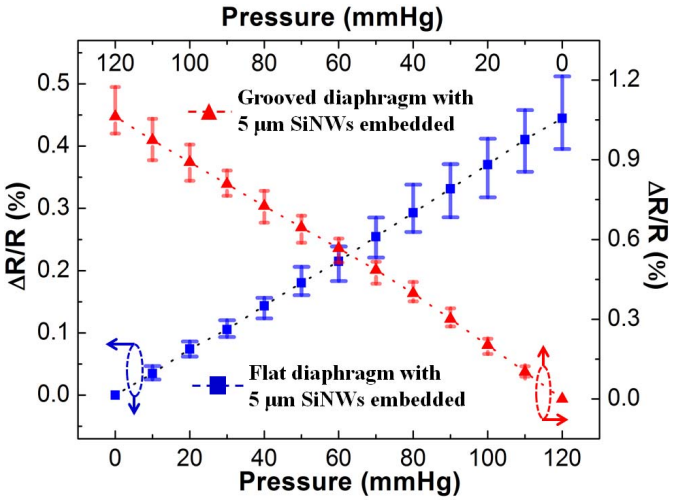

Fig. 8. Plot of output resistance variations with the blue curve and error bars for the flat diaphragm pressure sensor (refer to bottom X-and left Y-axis) and the red curve and error bars (refer to top X-and right Y-axis) for the grooved diaphragm pressure sensor with 5 μm SiNWs embedded in both cases.

The location of 1 μm SiNWs can be re-adjusted to completely within the high stress region. This will further improve the piezoresistance changes by ~40 % due to the reported higher gauge factor (G) of 1 μm SiNWs (G ~100) over that of 5 μm design (G ~ 65) [60]. The orientation of shorter SiNWs can also be re-aligned along the tangential direction [T-direction as defined in Fig. 1 (b)] without increasing the width of rib. As a result, further sensitivity enhancement will be achieved due to a relatively uniform average stress along the tangential direction at the narrow rib. In addition, non-linearity components will also be compensated among piezoresistors, when they are subjected to lateral stress [67]. Furthermore, the dimension and thickness of both rib and groove can be refined for a higher stress distribution profile and lower non-linearity.

C. Temperature Effects

Temperature variation is another key factor, which affects several parameters like material property, feature geometry and mostly importantly the piezoresistive effect [2], [11], [12]. The contribution from other temperature dependent factors varies and is relatively smaller compared with that from the piezoresistor itself [30]. For the p-type piezoresistor, the reported experimental result reveals the dependency of shear piezoresistance coefficient on both impurity concentrations and temperature variations [16], [18]. A more general expression for the relationship between the pieozresistance and its temperature dependency is defined by Y. Kanda [65] as:

$$\prod(N,T) = P(N,T) * \prod(300) \tag{7}$$

Where $\Pi(N,T)$ is the piezoresistance coefficient with an impurity concentration N at a temperature T. $\Pi(300)$ is the piezoresistance coefficient at temperature of 300 K. $P(N,T)$ is the piezoresistance factor and can be expressed as:

$$P(N,T) = \frac{300}{T\ln(1+e^{E_f/kT})(1+e^{-E_f/kT})} \tag{8}$$

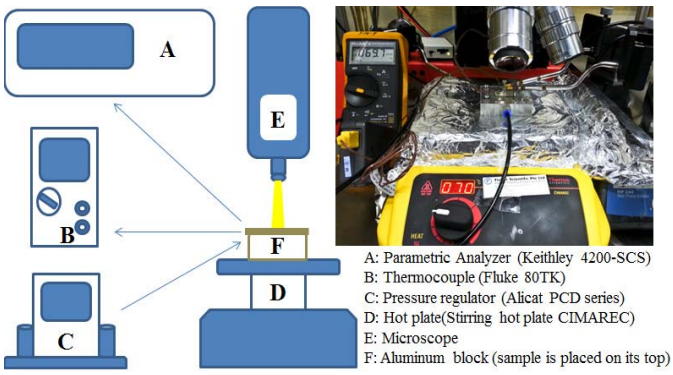

Fig. 9. Illustration of setups for the temperature response test of the reported pressure sensor.

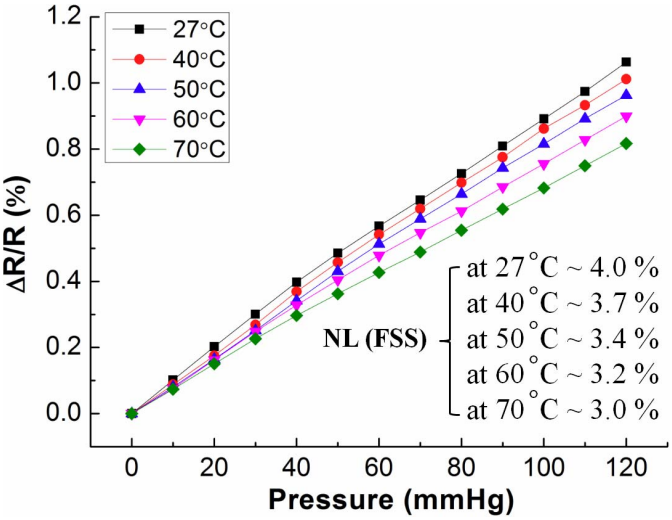

Fig. 10. Output resistance changes under different ambient temperatures (27 °C to 70 °C). The plotted data is measured from reported groove diaphragm pressure sensors with 5μm long SiNWs as piezoresistors. Insets show the non-linearity (NL) component with respect to outputs at different temperatures.

Where, the E_f is the Fermi energy and it is related to the impurity concentration. It has been reported that equation (7) may be suitable for the first-order approximation and the simulated result matches the experimental data in case of pure circular and square diaphragm based pressure sensors [30]. In order to explore the temperature response of our device, the hot plate is used as the heat source. Temperature changes are monitored by thermocouple with accuracy around ±2 °C of its display value. The device is assembled on top of an aluminum block by an acrylic plate. The gasket is used to surround the testing sample for air sealing purpose. The air pressure is applied from the backside of the test sample by a pressure regulator (The similar Al sealing block has also been reported in [64]). The electrical path is established by probing bonding pads through a small opening window on the acrylic plate and resistance changes are recorded by the parametric analyzer. The detailed setup is shown in Fig. 9.

The response of the device is examined within temperatures varying from 27 °C (room temperature) to 70 °C, which is a reasonable temperature range for most bio-medical related

TABLE II
THE COMPARISON OF BIO-MEDICAL PIEZORESISTIVE PRESSURE SENSING DEVICES BETWEEN THIS WORK AND OTHER REPORTED DESIGN

Ref.	Applications of sensing	Sensing element	Effective sensing area (μm^2)	Sensitivity *((ΔR/R)/mmHg)*	Normalized Sensitivity *((ΔR/R)/mmHg/μm²)*
[68]	Intracranial pressure	P-doped polysilicon wires	$\pi * 500^2 = 785398$	$\sim 13 \times 10^{-5}$	$\sim 1.66 \times 10^{-10}$
[10]	Cardiovascular blood pressure	P-doped silicon wires	$600 * 600 = 360000$	$\sim 4 \times 10^{-5}$	$\sim 1.1 \times 10^{-10}$
[9]	Coronary blood pressure	Polysilicon strain gauge	$100 * 100 = 10000$	$\sim 0.07 \times 10^{-5}$	$\sim 0.7 \times 10^{-10}$
[69]	Intraocular pressure	NiCr	$5400 * 5400 = 29160000$	$\sim 80.8 \times 10^{-5}$	$\sim 0.28 \times 10^{-10}$
Previous work [60] (1 μm SiNWs)	Other application	P-doped SiNWs	$\pi * 100^2 = 31416$	$\sim 5 \times 10^{-5}$	$\sim 15.9 \times 10^{-10}$
This work (5 μm SiNWs)	low pressure for bio-medical purpose	P-doped SiNWs	$\pi * 100^2 = 31416$	$\sim 8.92 \times 10^{-5}$	$\sim 28.4 \times 10^{-10}$

applications. The tip portion of the thermocouple is closely attached on the top surface of the aluminum block (just beside the test sample). Once the reading from the thermocouple is stabilized, another 20 minutes interval is spent before tightening the acrylic plate by screws. This minimizes any testing errors introduced by the setup. Additionally, the entire hot plate is covered with aluminum foils, which is connected to the common ground, to reduce the noise signal generated from the testing instrument. The temperature testing result of the grooved pressure sensor with 5 μm SiNWs is plotted in Fig. 10. The obvious sensitivity drop over temperature increment is reported. Compared with the output resistance change at room temperature (27 °C), this drop of output performance is as large as 23% at 70 °C. Contrary to the sensitivity degradation, the linearity component improves at higher temperature. Based on equation (5), the non-linearity under the full scale span is around 3% (shown in the set of Fig. 10) at 70 °C. Such temperature dependent linearity change is in a good agreement with the literature [25].

V. CONCLUSION

To provide a clearer view for the performance of the grooved diaphragm based SiNWs sensing device under a low pressure, especially for bio-medical applications, a comparison is tabulated in Table II with all references reported for different bio-medical applications except our previous work. It is shown in Table II that our reported SiNWs based devices demonstrate the great scalability (indicated in column 4). The sensitivity $((\Delta R/R)$/mmHg) for all devices is also summarized in column 5. It seems that the performance is highly dependent on the area of sensing diaphragm. In fact, the relationship between the effective sensing area and the device sensitivity should be linearly proportional as predicted by the plate theory [34]. Thus, a fair sensitivity comparison among all types of pressure sensing devices is listed in the last column of the table. After normalizations of variations in the effective sensing area, the sensitivity improvement of the previously reported flat diaphragm based SiNWs pressure sensor is almost an order over other literature reports. With a further improvement benefited by the groove structure, the currently reported device boosts up the sensitivity by at least 17 times compared with results reported by other groups. Such significant improvement proves the feasibility for implementing SiNWs based device for low pressure sensing applications by simply reconfiguring the device diaphragm.

In summary, the new annularly grooved diaphragm pressure sensor with SiNWs embedded as a piezoresistor is reported here. Various design considerations for both sensitivity improvement and minimization of nonlinearity have been discussed in detail. Experimental results are summarized and analyzed with respect to results from the previous flat diaphragm based SiNWs pressure sensor. Both FEM and measurement data explain the benefit of the groove structure that forces the stress to be concentrated around the rib region and results in a greater resistance change. The performance variation of the device over a reasonable temperature range is examined. A table is also summarized with an explicit indication for the enhancement of SiNWs based devices over other reported traditional piezoresistive pressure sensors. Benefiting by the superiority of SiNWs, the reported proof-of-concept device with the groove diaphragm structure further enhances the sensing capability and fulfills the demand for working under the low pressure range required by implantable bio-medical applications.

REFERENCES

[1] C. S. Smith, "Piezoresistance effect in germanium and silicon," *Phys. Rev.*, vol. 94, no. 1, pp. 42–49, 1954.
[2] Y. Kanda, "Piezoresistance effect in silicon," *Sens. Actuators A, Phys.*, vol. 28, no. 2, pp. 83–91, 1991.
[3] J. Richter, O. Hansen, A. Nylandsted Larsen, J. Lundsgaard Hansen, G. F. Eriksen, and E. V. Thomsen, "Piezoresistance of silicon and strained Si0.9Ge0.1," *Sens. Actuators A, Phys.*, vols. 123–124, pp. 388–396, Sep. 2005

[4] K. E. Petersen, "Silicon as a mechanical material," *Proc. IEEE*, vol. 70, no. 5, pp. 420–457, Jan. 1982.

[5] S. K. Clark and K. D. Wise, "Pressure sensitivity in anisotropically etched thin-diaphragm pressure sensors," *IEEE Trans. Electron Devices*, vol. 26, no. 12, pp. 1887–1896, Dec. 1979.

[6] L. Lin and W. Yun, "Design, optimization and fabrication of surface micromachined pressure sensors," *Mechatronics*, vol. 8, no. 5, pp. 505–519, 1998.

[7] G. Yoshikawa, T. Akiyama, S. Gautsch, P. Vettiger, and H. Rohrer, "Nanomechanical membrane-type surface stress sensor," *Nano Lett.*, vol. 11, no. 3, pp. 1044–1048, 2011.

[8] H.-S. Hsieh, H.-C. Chang, C.-F. Hu, C.-L. Cheng, and W. Fang, "A novel stress isolation guard-ring design for the improvement of a three-axis piezoresistive acceleromete," *J. Micromech. Microeng.*, vol. 21, no. 10, p. 105006, 2011.

[9] J. Liu, J. Wang, and X. Li, "Fully front-side bulk-micromachined single-chip micro flow sensors for bare-chip SMT (surface mounting technology) packaging," *J. Micromech. Microeng.*, vol. 22, no. 3, p. 035020, 2012.

[10] C. Herring and E. Vogt, "Transport and deformation-potential theory for many-vally semiconductor with anisotripic scatterring," *Phys. Rev.*, vol. 101, pp. 944–961, Feb. 1956

[11] G. E. Pikus and G. L. Bir, "Effect of deformation on the hole energy spectrum of germanium and silicon," *Sov. Phys. Solid State*, vol. 1, no. 1, pp. 1502–1517, 1960.

[12] T. Toriyama and S. Sugiyama, "Analysis of piezoresistance in p-type silicon for mechanical sensors," *J. Microelectromech. Syst.*, vol. 11, no. 5, pp. 598–604, 2002.

[13] S. I. Kozlovskiy and I. I. Boiko, "First-order piezoresistance coefficients in silicon crystals," *Sens. Actuators A, Phys.*, vol. 118, no. 1, pp. 33–43, 2005.

[14] S. I. Kozlovskiy, V. V. Nedostup, and I. I. Boiko, "First-order piezoresistance coefficients in heavily doped p-type silicon crystals," *Sens. Actuators A, Phys.*, vol. 133, no. 1, pp. 72–81, 2007.

[15] F. J. Morin, T. H. Geballe, and C. Herring, "Temperaure dependance of the piezoresistance of high-purity silicon and germanium," *Phys. Rev.*, vol. 105, no. 2, pp. 525–539, 1957.

[16] O. N. Tufte and E. L. Stelzer, "Piezoresistive properties of silicon diffused layers," *J. Appl. Phys.*, vol. 34, no. 2, pp. 313–318, 1963.

[17] J. T. Lenkkeri, "Nonlinear effects in the piezoresistivity of p-type silicon," *Phys. Status Solidi (b)*, vol. 136, no. 1, pp. 373–385, 1986.

[18] J. Richter, J. Pedersen, M. Brandbyge, E. V. Thomsen, and O. Hansen, "Pieozresistance in p-type silicon revisited," *J. Appl. Phys.*, vol. 104, no. 2, p. 023715, 2008.

[19] W. Jiachou, X. Xiaoyuan, and L. Xinxin, "Monolithic integration of pressure plus acceleration composite TPMS Sensors with a single-sided micromachining technology," *J. Microelectromech. Syst.*, vol. 21, no. 2, pp. 284–293, 2012.

[20] Q. Wang, X. Li, T. Li, M. Bao, and W. Zhou, "On-chip integration of acceleration, pressure, and temperature composite sensor with a single-sided micromachining technique," *J. Microelectromech. Syst.*, vol. 20, no. 1, pp. 42–52, 2011.

[21] K. H. Kim, B. H. Kim, and Y. H. Seo, "A noncontact intraocular pressure measurement device using a micro reflected air pressure sensor for the prediagnosis of glaucoma," *J. Micromech. Microeng.*, vol. 22, no. 3, p. 035022, 2012.

[22] P. Melvas and G. Stemme, "A diode-based two-wire solution for temperature-compensated piezoresistive pressure sensors," *IEEE Trans. Electron Devices*, vol. 50, no. 2, pp. 503–509, Feb. 2003.

[23] S. Marco, J. Samitier, O. Ruiz, J. R. Morante, and J. Esteve, "High-performance piezoresistive pressure sensors for biomedical applications using very thin structured membranes," *Meas. Sci. Technol.*, vol. 7, no. 9, p. 1195, 1996.

[24] O. N. Tufte, P. W. Chapman, and D. Long, "Silicon diffused-element piezoresistive diaphragms," *J. Appl. Phys.*, vol. 33, no. 11, pp. 3322–3327, 1962.

[25] M. Shimazoe *et al.*, "A special silicon diaphragm pressure sensor with high output and high accuracy," *Sens. Actuators A, Phys.*, vol. 2, pp. 275–282, Jan. 1982.

[26] H. Sandmaier, "Non-linear analytical modelling of bossed diaphragms for pressure sensors," *Sens. Actuators A, Phys.*, vol.27, nos. 1–3, pp. 815–819, 1991.

[27] M. Bao, L. Yu, and Y. Wang, "Stress concentration structure with front beam for pressure sensor," *Sens. Actuators A, Phys.*, vol. 28, no. 2, pp. 105–112, 1991.

[28] B. Min-Hang, Y. Lian-Zhong, and W. Yan, "Micromachined beam-diaphragm structure improves performances of pressure transducer," *Sens. Actuators A, Phys.*, vol. 21, nos. 1–3, pp. 137–141, 1990.

[29] R. H. Johnson, S. Karbassi, U. Sridhar, and B. Speldrich, "A high-sensitivity ribbed and bossed pressure transducer," *Sens. Actuators A, Phys.*, vol. 35, no. 2, pp. 93–99, 1992.

[30] L. Liwei, C. Huey-Chi, and Y.-W. Lu, "A simulation program for the sensitivity and linearity of piezoresistive pressure sensors," *J. Microelectromech. Syst.*, vol. 8, no. 4, pp. 514–522, 1999.

[31] K. Matsuda, Y. Kanda, K. Yamamura, and K. Suzuki, "Nonolinearity of piezoresistance effect in p- and n-type silicon," *Sens. Actuators A, Phys.*, vol. 21, no. 1, pp. 45–48, 1990

[32] L. Lin and W. Yun, "Design, optimization and fabrication of surface micromachined pressure sensors," *Mechatronics*, vol. 8, no. 5, pp. 505–519, 1998.

[33] S. Marco, J. Samitier, O. Ruiz, J. R. Morante, and J. Esteve, "Analysis of nonlinearity in high sensitivity piezoresistive pressure sensors," *Sens. Actuators A, Phys.*, vols. 37–38, no. 1, pp. 790–795, 1993.

[34] W. Krieger, *Theory of Plates and Shells*, 2nd ed. New York, NY, USA: McGraw-Hill, 1970.

[35] B. Soree, W. Magnus, and W. Vandenberghe, "Low-field mobility in ultrathin silicon nanowire junctionless transsistors," *Appl. Phys. Lett.*, vol. 99, no. 23, p. 233509, 2011

[36] H. Carrillo-Nunez *et al.*, "Phonon-assisted Zener tunneling in a cylindrical nanowire transistor," *J. Appl. Phys.*, vol. 113, no. 18, p. 184507, 2013.

[37] C. S. Roper, A. Gutés, C. Carraro, R. T. Howe, and R. Maboudian, "Single crystal silicon nanopillars, nanoneedles and nanoblades with precise positioning for massively parallel nanoscale device integration," *Nanotechnol.*, vol. 23, no. 22, p. 225303, 2012.

[38] T. Tsuchiya, Y. Ura, K. Sugano, and O. Tabata, "Electrostatic tensile testing device with nanonewton and nanometer resolution and its application to nanowire testing," *J. Microelectromech. Syst.*, vol. 21, no. 3, pp. 523–529, 2012.

[39] P. Ginet, S. Akiyama, N. Takama, H. Fujita, and B. Kim, "CMOS-compatible fabrication of top-gated field-effect transistor silicon nanowire-based biosensors," *J. Micromech. Microeng.*, vol. 21, no. 6, p. 065008, 2011.

[40] C.-F. Hu, W.-S. Su, and W. Fang, "Development of patterned carbon nanotubes on a 3D polymer substrate for the flexible tactile sensor application," *J. Micromech. Microeng.*, vol. 21, no. 11, p. 115012, 2011.

[41] X. Yu *et al.*, "Top-down fabricated silicon-nanowire-based field-effect transistor device on a (111) silicon wafer," *Small*, vol. 9, no. 4, pp. 525–530, 2013.

[42] D. Van Thanh *et al.*, "A micromirror with CNTs hinge fabricated by the integration of CNTs film into a MEMS actuator," *J. Micromech. Microeng.*, vol. 23, no. 1, pp. 075024-1–075024-6, 2013.

[43] R. R. He and P. D. Yang, "Giant piezoresistance effect in silicon nanowires," *Nature Nanotechnol.*, vol. 1, no. 1, pp. 42–46, 2006.

[44] A. Koumela *et al.*, "Piezoresistance of top-down suspended Si nanowires," *Nanotechnol.*, vol. 22, no. 39, p. 395701, 2011.

[45] J. S. Milne, A. C. H. Rowe, S. Arscott, and C. Renner, "Giant Piezoresistance Effects in Silicon Nanowires and Microwires," *Phys. Rev. Lett.*, vol. 105, no. 22, p. 226802, 2010.

[46] T.-K. Kang, "Evidence for giant piezoresistance effect in n-type silicon nanowire field-effect transistors," *Appl. Phys. Lett.*, vol. 100, no. 16, p. 163501, 2012.

[47] H. D. Tong, S. Chen, W. G. van der Wiel, E. T. Carlen, and A. van den Berg, "Novel top-down wafer-scale fabrication of single crystal silicon nanowires," *Nano Lett.*, vol. 9, no. 3, pp. 1015–1022, 2009.

[48] J. Xiang, W. Lu, Y. Hu, Y. Wu, H. Yan, and C. M. Lieber, "Ge/Si nanowire heterostructures as high-performance field-effect transistors," *Nature*, vol. 441, no. 7092, pp. 489–493, 2006.

[49] L. Lou, W. T. Park, S. Zhang, L. S. Lim, D. L. Kwong, and C. Lee, "Characterization of silicon nanowire embedded in a MEMS diaphragm structure within large compressive strain range," *IEEE Electron Device Lett.*, vol. 32, no. 12, pp. 1764–1766, Dec. 2011.

[50] B. Soree *et al.*, "Novel device concepts for nanotechnology: The nanowire pinch-off FET and graphene tunnel FET," *ECS Trans.*, vol. 28, pp. 15–26, Jan. 2010.

[51] Y. Zhang, X. Liu, C. Ru, Y. L. Zhang, L. Dong, and Y. Sun, "Piezoresistivity characteriztion of Synthetic silicon nanowires using a MEMS device," *J. Microelectromech. Syst.*, vol. 20, no. 4, pp. 959–966, 2011.

[52] L. K. Tymon Barwicz, S. J. Koester, and H. Hamann, "Silicon nanowire piezoresistance: Impact of surface crystallographic orientation," *Appl. Phys. Lett.*, vol. 97, no. 2, p. 023110, 2010.

[53] T. Ikehara and T. Tsuchiya, "Low-cycle to ultrahigh-cycle fatigue lifetime measurement of single-crystal-silicon specimens using a microresonator test device," *J. Microelectromech. Syst.*. vol. 21, no. 4, pp. 830–839, 2012.
[54] L. Liang, H. Yan, W.-T. Park, D.-L. Kwong, and C. Lee, "Characterization of piezoresistive-Si-nanowire-based pressure sensors by dynamic cycling test with extralarge compressive strain," *IEEE Trans. Electron Devices*, vol. 59, no. 11, pp. 3097–3103, Nov. 2012.
[55] A. A. Barlian, W.-T. Park, J. R. Mallon, A. J. Rastegar, and B. L. Pruitt, "Review: Semiconductor piezoresistance for microsystems," *Proc. IEEE*, vol. 97, no. 3, pp. 513–552, Mar. 2009.
[56] T. Toriyama, Y. Tanimoto, and S. Sugiyama, "Single crystal silicon nanowire piezoresistors for mechanical sensor," *J. Microelectromech. Syst.*, vol. 11, no. 5, pp. 605–611, 2002.
[57] W.-T. Park, R. K. Kotlanka, L. Lou, M. Hamidullah, and C. Lee, "MEMS tri-axial force sensor with an integrated mechanical stopper for guidewire applications," *Microsyst. Technol.*, vol. 19, no. 7, pp. 1005–1015, 2013.
[58] S. Zhang, L. Lou, and C. Lee, "Piezoresistive silicon nanowire based nanoelectromechanical system cantilever air flow sensor," *Appl. Phys. Lett.*, vol. 100, no. 2, pp. 023111-1–023111-3, 2012.
[59] Y. Qian, L. Lou, M. J. Tsai, and C. Lee, "A dual-silicon-nanowires based U-shape nanoelectromechanical switch with low pull-in voltage," *Appl. Phys. Lett.*, vol. 100, no. 11, pp. 113102-1–113102-3, 2012.
[60] L. Lou, S. Zhang, W. T. Park, J. M. Tsai, D. L. Kwong, and C. Lee, "Optimization of NEMS pressure sensors with a multilayered diaphragm using silicon nanowires as piezoresistive sensing element," *J. Micromech. Microeng.*, vol. 22, no. 5, p. 055012, 2012.
[61] A. Yasukawa, M. Shimazoe, and Y. Matsuoka, "Simulation of circular silicon pressure sensors with a center boss for very low pressure measurement," *IEEE Trans Electron Devices*, vol. 36, no. 7, pp. 1295–1302, Jul. 1989.
[62] A. J. Chiou and S. Chen, "Pressure nonlinearity of micromachined piezoresistive pressure sensors with thin diaphragms under high residual stresses," *Sens. Actuators A, Phys.*, vol. 147, no. 1, pp. 332–339, 2008.
[63] K. Yamada, M. Nishihara, S. Shimada, M. Tanabe, M. Shimazoe, and Y. Matsuoka, "Nonlinearity of the piezoresistance effect of p-type silicon diffused layers," *IEEE Trans. Electron Devices*, vol. 29, no. 1, pp. 71–77, Jan. 1982.
[64] S. Zhang, L. Lou, W.-T. Park, and C. Lee, "Characterization of a silicon nanowire-based cantilever air-flow sensor," *J. Micromech. Microeng.*, vol. 22, no. 9, p. 095008, 2012.
[65] Y. Kanda, "A graphical representation of the piezoresistance coefficients in silicon," *IEEE Trans. Electron Devices*, vol. 29, no. 1, pp. 64–70, Jan. 1982.
[66] S. Beeby, G. Ensell, M. Kraft, and N. White, *MEMS—Electromechanical Sensors*, 2nd ed. Norwood, MA, USA: Artech House, 2004.
[67] J. Mallon, F. Pourahmadi, K. Petersen, P. Barth, T. Vermeulen, and J. Brezek, "Low-pressure sensors employing bossed diaphragms and precision etch-stopping," *Sens. Actuators A, Phys.*, vols. 21–23, pp. 89–95, Jan. 1990.
[68] Z. Wu, C. Li, J. A. Hartings, R. K. Narayan, and C. H. Ahn, "A new intracranial pressure sensor on polyimide lab-on-a-tube using exchanged polysilicon piezoresistors," in *Proc. 17th Int. Conf. Solid-State Sens., Actuators, Microsyst.*, Barcelona, Spain, Jun. 2013, pp. 1779–1782.
[69] B. Bae, K. Bark, and M. A. Shannon, "Low-pressure treatment control of glaucoma using an electromagnetic valve actuator with a piezoresistive pressure sensor," in *Proc. 3rd IEEE/EMBS Special Topic Conf. Microtechnol. Med. Biol.*, May 2005, pp. 126–129.

Songsong Zhang received the B.Tech. degree from the Department of Electrical and Computer Engineering, National University of Singapore, Singapore, in 2009, where he is currently working toward the Ph.D. degree in electrical engineering.

His research work is on development of the SiNWs-based NEMS mechanical sensors for biomedical applications and neural prosthetics devices.

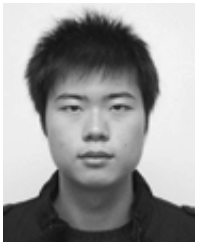

Tao Wang received his B.Eng. degree from the School of Microelectronics and Solid-State Electronics at the University of Electronic Science and Technology of China (UESTC), Chengdu, China, in 2010, and M.Sc. degree from Department of Electrical and Computer Engineering at the National University of Singapore, in 2011.

He is now a Ph.D. student in Electrical & Computer Eng. Dept., NUS. His research interests are focused on ZnO-based MEMS devices.

Liang Lou received his B.Eng. degree from the Department of Electronic Engineering and Information Science, University of Science and Technology of China, Hefei, Anhui, China, in 2008. He went on to receive his Ph.D. degree from the Department of Electrical & Computer Engineering at the National University of Singapore in 2012.

He is currently a Research Scientist at the Institute of Microelectronics (IME), A*STAR. His research interests include nanowire-based MEMS and NEMS sensors.

Wei Mong Tsang (M'10) received the B. Eng. (first class Honors) and M. Phil. degrees in electronic engineering from the Chinese University of Hong Kong, Hong Kong, in 2000 and 2002, respectively, and the Ph.D. degree in electrical and electronic engineering from the University of Surrey, Guildford, U.K., in 2007.

He was a Postdoctoral associated in the Research Laboratory of Electronic, Massachusetts Institute of Technolgy, Cambridge. He is currently a Research Scientist at the Institute of Microelectronics (IME), A*STAR. His research interests include the bio micro electro mechanical systems, neural prosthetics, and electron field emission.

Renshi Sawada received the B.E., M.E., and Ph.D. degrees from Kyushu University, Fukuoka, Japan, in 1976, 1978, and 1995, respectively. In 1978, he joined the Electrical Communication Laboratories, Nippon Telegraph and Telephone, Tokyo, Japan. Since January 2004, he has been at Kyushu University, Fukuoka, Japan. He is an Editor of the *Journal of Micromechanics and Microengineering* and has served as member of the board of trustees, including JIEP in 2008-2010, the Society of Instrument and Control Engineers in 2006-2007, and the Kyushu branch of the Japanese Society for Medical and Biological Engineering since 2009. He received the Japan Society of Precision Engineering Awards in 1981 and 1991; the Okawa Press Prize in 2001; the 9th Microoptics Conference (MOC) Paper Prize in 2003; the Japan Institute of Electronic Packaging Awards in 2010; and the Best Paper Award in Sensordevices of International Academy, Research, and Industry Association (IARIA). He also served as conference chair for a number of international conferences, including IEEE International Optical MEMS Conference in 2000 and 2001, was also involved in Program Committees of many conferences, and is a Fellow of the Institute of Physics.

Dim-Lee Kwong (F'09) received the B.S. degree in physics and the M.S. degree in nuclear engineering from the National Tsing Hua University, Hsinchu, Taiwan, in 1977 and 1979, respectively. He received the Ph.D. degree in electrical engineering from Rice University, Houston, TX, in 1982. He is the Executive Director of the Institute of Microelectronics (IME), Agency for Science, Technology, and Research, Singapore; a Professor of electrical and computer engineering with the National University of Singapore, Singapore; and an Adjunct Professor of electrical and computer engineering with the University of Texas at Austin. He was the Earl N. and Margaret Bransfield Endowed Professor with the University of Texas at Austin from 1990 to 2007, and the Temasek Professor with the National University of Singapore from 2001 to 2004. He is the author of more than 1000 refereed archival publications (560 journal and 470 conference proceedings), has presented more than 80 invited talks at international conferences, and is the holder of more than 25 U.S. patents. He was the Founder of Rapro Technology Inc., in 1986, and Micro Integration Corporation, in 1988, and has been a Consultant to government research laboratories, semiconductor IC manufacturers, and materials and equipment suppliers in the U.S. and overseas. Prof. Kwong was the recipient of the IBM Faculty Award from 1984 to 1986, the Semiconductor Research Corporation Inventor Awards from 1993 to 1994, the General Motor Foundation Fellowship from 1992 to 1995, the Halliburton Foundation Excellent Teaching Award in 1994, the Engineering Foundation Award in 1995, the IEEE George Smith Award in 2007, and the 2011 IEEE Frederik Philips Award for leadership in silicon technology and excellence in the management of microelectronics R&D.

Chengkuo Lee (S'93 -M'96) received the M.S. degree in materials science and engineering from the National Tsing Hua University, Hsinchu, Taiwan, in 1991; the M.S. degree in industrial and system engineering from Rutgers University, New Brunswick, NJ, in 1993; and the Ph.D. degree in precision engineering from the University of Tokyo, Tokyo, Japan, in 1996. He worked as a Foreign Researcher in the Nanometerscale Manufacturing Science Laboratory of the Research Center for Advanced Science and Technology, University of Tokyo, from 1993 to 1996. He has also worked in the Mechanical Engineering Laboratory, AIST, MITI of Japan as a JST Research Fellow in 1996. Thereafter, he became a Senior Research Staff Member of the Microsystems Laboratory, Industrial Technology Research Institute, Hsinchu, Taiwan. In September 1997, he joined Metrodyne Microsystem Corporation, Hsinchu, Taiwan, and established the MEMS device division and the first micromachining fab for commercial purposes in Taiwan. He was the Manager of the MEMS device division between 1997 and 2000. He was an Adjunct Assistant Professor in the Electrophysics Department of the National Chiao Tung University, Hsinchu, Taiwan, in 1998, and an Adjunct Assistant Professor at the Institute of Precision Engineering of National Chung Hsing University, Taichung, Taiwan, from 2001 to 2005. In August 2001, he cofounded Asia Pacific Microsystems, Inc. (APM), where he first became Vice President of R&D before becoming Vice President of the optical communication business unit and Special Assistant to the Chief Executive Officer in charge of international business and technical marketing for the MEMS foundry service. From 2006 to 2009, he was a Senior Member of the Technical Staff at the Institute of Microelectronics, A-STAR, Singapore. Currently he is an associate Professor in the Department of Electrical and Computer Engineering, National University of Singapore, Singapore. He is the coauthor of *Advanced MEMS Packaging* (McGraw-Hill, 2010). He has contributed to more than 200 international conference papers and extended abstracts, and 150 peer-reviewed international journal articles in the fields of Sensors, Actuators, Energy Harvesting, MEMS, NEMS, nanophotonics, and nanotechnology. He is also the holder of nine U.S. patents.